Ceramics International 50 (2024) 4609–4621

Contents lists available at ScienceDirect

Ceramics International

journal homepage: www.elsevier.com/locate/ceramint

Fabrication, oxidation and creep behavior of Ti_2AlN composites

Xiaoqiang Li [a,*], Jia Qi [a], Egbert Wessel [a], Jesus Gonzalez-Julian [a,b], Ruth Schwaiger [a,c], Jürgen Malzbender [a]

[a] Forschungszentrum Jülich GmbH, Institute of Energy and Climate Research, 52425, Jülich, Germany
[b] Chair of Ceramics, Institute of Mineral Engineering, RWTH Aachen University, 52074, Aachen, Germany
[c] Chair of Energy Engineering Materials, Faculty 5, RWTH Aachen University, 52056, Aachen, Germany

ARTICLE INFO

Handling Editor: Dr P. Vincenzini

Keywords:
MAX phase
Ti_2AlN
Fabrication
Creep
Oxidation

ABSTRACT

In order to enhance the limited information on elevated temperature stability of MAX phase materials, Ti_2AlN MAX phase composites were fabricated in a two-step procedure and subsequently tested regarding their oxidation and creep behavior. Furthermore, commentary testing on material enhanced with different amount of Al_2O_3 fibers was performed. The compressive creep was investigated in the temperature range of 900–1200 °C under stresses ranging from 20 to 100 MPa, with a loading direction parallel and perpendicular to the compression direction during sintering. The oxidation behavior was characterized, demonstrating excellent oxidation resistance of the samples up to 1200 °C. Supported by microstructural investigations, the impact of the texturing of the matrix grains, the content and the orientation of Al_2O_3 fibers, as well as that of the interfaces between matrix grains and the Al_2O_3 fibers were investigated. De-cohesion and cracks formed at the triple junctions of the MAX phase grains indicate grain boundary sliding as predominant creep mechanism for the composites.

1. Introduction

Ti_2AlN belongs to a family of metal-ceramic layered ternary carbides and nitrides, referenced as MAX Phases, with the general formula of $M_{n+1}AX_n$ (n = 1, 2, 3), where "M" is an early transition element, "A" represents elements of group IIIA to VIA and "X" corresponds to either C or N [1,2]. Due to the layered hexagonal crystal structure composed of alternately stacking of M-X octahedron and weakly bonded A slabs, MAX phases exhibit some ceramic-like properties, such as low density, high elastic modulus, and some of them excellent oxidation and corrosion resistance at high temperature, meanwhile they possess also some metallic characteristics, for example high electrical and thermal conductivities, good thermal shock resistance and damage tolerance, as well as good machinability [1,3,4]. In particular, Ti_2AlN is a member of aluminum-containing MAX phases, which has high potential due to its excellent oxidation and corrosion resistance at high temperature related to the in-situ formation of an external, protective and well-adhered α-Al_2O_3 layer [5,6]. Hence, Ti_2AlN might be considered as promising candidate as a structural material in aggressive environments.

High temperature oxidation and creep behavior are critical, application relevant aspects. In addition, a promising and widely used solution to improve the mechanical performance of monolithic ceramics is the introduction of fibers [7–15], which is a complementary aspect, where investigations on the fabrication of fiber reinforced nitride MAX phase materials have not yet been reported. The chemical stability should be taken into consideration for the design of the fiber/MAX phase materials, especially for the long-term application at high temperatures under oxidizing atmospheres [15]. Typically, Al_2O_3 fibers are chemically stable with aluminum-containing MAX phases due to the easy diffusion of aluminum at elevated temperatures [15]. Moreover, considering the principle of modulus matching and the excellent mechanical properties, high-modulus alumina (Al_2O_3) fibers have been used to prepare ceramic matrix composites (CMC) with apparently good mechanical properties [16]. In addition, the dry mixing of chopped fibers and ceramic powders offers a low cost and time-saving approach to incorporate reinforcing fibers into a CMC, thus avoiding brittle fracture and catastrophic failure of the material [13]. Short Al_2O_3 fiber/Ti_2AlN composites represent a promising strategy to improve the overall mechanical behavior of the Ti_2AlN material.

Typically creep resistance of structural materials, one of the most important thermomechanical characteristics at elevated temperatures, quantifies the permanent deformation and ultimately damage, thus

* Corresponding author.
E-mail address: xi.li@fz-juelich.de (X. Li).

https://doi.org/10.1016/j.ceramint.2023.11.205
Received 7 September 2023; Received in revised form 31 October 2023; Accepted 16 November 2023
Available online 19 November 2023

Table 1
Conditions of the compressive creep test on Al_2O_3 fiber/Ti_2AlN composites.

Geometry (mm^2)	Temperature (°C)	Stress (MPa)				
⌀ 5 × 7	900		40	60	80	100
	1000	20	40	60	80	100
	1100	20	40	60	80	
	1200	20	40	60		

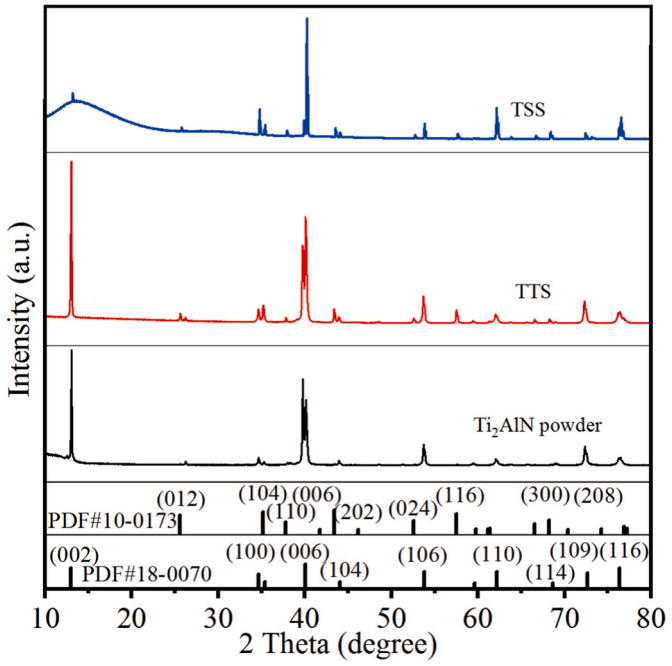

Fig. 1. 2 theta-theta scan of the as-synthesized Ti_2AlN powder and as-obtained 20ATN specimens showing the high purity of as-synthesized Ti_2AlN powder and clear differences of grain distribution between TTS and TSS for 20ATN materials.

permitting evaluation of the potential as high temperature materials under harsh service conditions [17]. However, works regarding the creep behavior of MAX phase based composites exist only to a limited extent [11,18–25], especially for nitride MAX phases [25].

The aim of the current work is to optimize parameters for the fabrication and characterize the high temperature properties of Ti_2AlN materials, with complementary studies on short Al_2O_3 fiber enhanced material with envisaged high homogeneity. In particular, also the application-relevant oxidation behavior was characterized. Furthermore, creep resistance at elevated temperatures of Ti_2AlN composites was characterized, and additionally material containing different amounts of chopped Al_2O_3 fibers with different alignments. This work will serve as a basis for a reference on the mechanical properties of this MAX phase material for potential applications at elevated temperatures giving an outlook on potential limits due to oxidation and creep behavior.

2. Experimental procedure

2.1. Materials preparation

Ti_2AlN powders were synthesized by liquid/solid state reaction at high temperature under argon atmosphere. Raw materials were titanium (99.5 % pure), aluminum (99.5 % pure) and titanium nitride (99.5 % pure) powders (all from Alfa Aesar, Germany) with a moral ratio of 1:1.1:1, that were mixed using manual shaking for 10 min. The powder mixture was heat treated under an argon atmosphere at 1400 °C, with a heating/cooling rate of 5 K/min and a dwelling time of 4 h. Afterwards, the as-synthesized Ti_2AlN powder was ball-milled using a planetary mill (PM400, Retsch GmbH, Germany) at 300 r.p.m for 2 h, where ZrO_2 milling balls with 5 mm diameters were used, using a powder-to-ball ratio of 1:2 in weight and ethanol as liquid media. After that, the as-obtained Ti_2AlN powder was dried in an oven at 60 °C for 24 h, followed by sieving through a 200 μm sieve.

Commercial continuous Al_2O_3 fiber (>99 wt % Al_2O_3, Nextel™ 610, 3 M, Maplewood, MN, USA) were chopped using a paper cutter to obtain short fibers with a length of approx. 1 mm. Afterwards, the short fibers were calcined at 750 °C in an Al_2O_3 crucible, with a heating rate of 5 K/min for 30 min, to remove the organic coatings on the surface that the commercial fibers contain.

In order to obtain Ti_2AlN composites containing different amounts of well distributed Al_2O_3 fibers, a NaCl salt-templated strategy was applied in the current work, similar as reported in our previous work [26]. Briefly, first, the hand-chopped Al_2O_3 fibers (0, 10, 20 vol %) were dispersed in ethanol in a beaker with ultrasonic support (VWR TM) to obtain a homogeneous dispersion. Then commercial NaCl powders (99 %, Alfa Aesar) were poured into the beaker, with a ratio in volume NaCl powder to fibers of 50:1. Afterwards, the mixture was magnetic stirred for 3 h, followed by addition of as-synthesized Ti_2AlN powders into the mixture of NaCl and hand-chopped Al_2O_3 fibers, and the stirring speed was kept at 350 r.p.m during the whole magnetic stirring procedure. After the stirring, the mixture of NaCl powders, hand-chopped Al_2O_3 fibers and Ti_2AlN powders were poured into a vacuum filter, then washed using deionized water to remove the NaCl powders. After washing several times, the remaining powder mixture was dried in an oven at 60 °C for 24 h. In addition, the NaCl solution after filtering were also dried at 60 °C in the oven for 3 days to recrystallize NaCl particles. The recycled NaCl particles were crushed in an agate mortal and sieved through 20 mesh for the next round mixing procedure.

The Ti_2AlN powder mixtures with a plate-like morphology, containing different amounts of short Al_2O_3 fibers, were densified via Field Assisted Sintering Technology/Spark plasma sintering (FAST/SPS) (FCT-HPD5, FCT Systeme GmbH, Germany). Details on the parameters can also be found in previous works [25,27]. Briefly, the mixture powders were poured into a graphite die with an inner diameter of 20 mm and pre-compacted under uniaxial pressure of 30 MPa for 60 s. Afterwards, a heating rate of 20 K/min with a pressure of 20 MPa from room temperature to 1000 °C was applied, followed by a heating rate of 50 K/min and a pressure of 40 MPa from 1000 °C to 1400 °C. Dwell time was 15 min. Thereby, finally bulk specimens were obtained. The surface (top surface) perpendicular and the surface (side surface) parallel to the compression direction are designated as TTS and TSS, respectively, in the following. In addition, the derived Ti_2AlN composites containing x vol. % ($x = 0$, 10 or 20) short Al_2O_3 fiber are termed xATN.

Before characterization, 400-4000-grid SiC sandpapers were used here to remove the contaminated layer being a result of the graphite foil used during the FAST/SPS procedure. In addition, the samples were cut and embedded in water-free epoxy resin, then ground with SiC sandpaper and polished with 3 μm, and subsequently 1 μm diamond polishing compound (MetaDi, BUEHLER) with colloidal silica suspension (50 nm Alkaline, CLOEREN TECHNOLOGY GmbH).

2.2. Thermogravimetric analysis

The oxidation resistance in air was evaluated using a Rigaku Thermo Plus TG8120 TGA instrument (Rigaku Corp., Tokyo, Japan) at a maximal temperature of 1200 °C, with a dwelling time of 2 h and a heating rate of 5 K/min, then followed by cool down to room temperature with a cooling rate of 5 K/min.

2.3. Compressive creep tests

In order to assess the impact of texturing of the matrix grains, as well

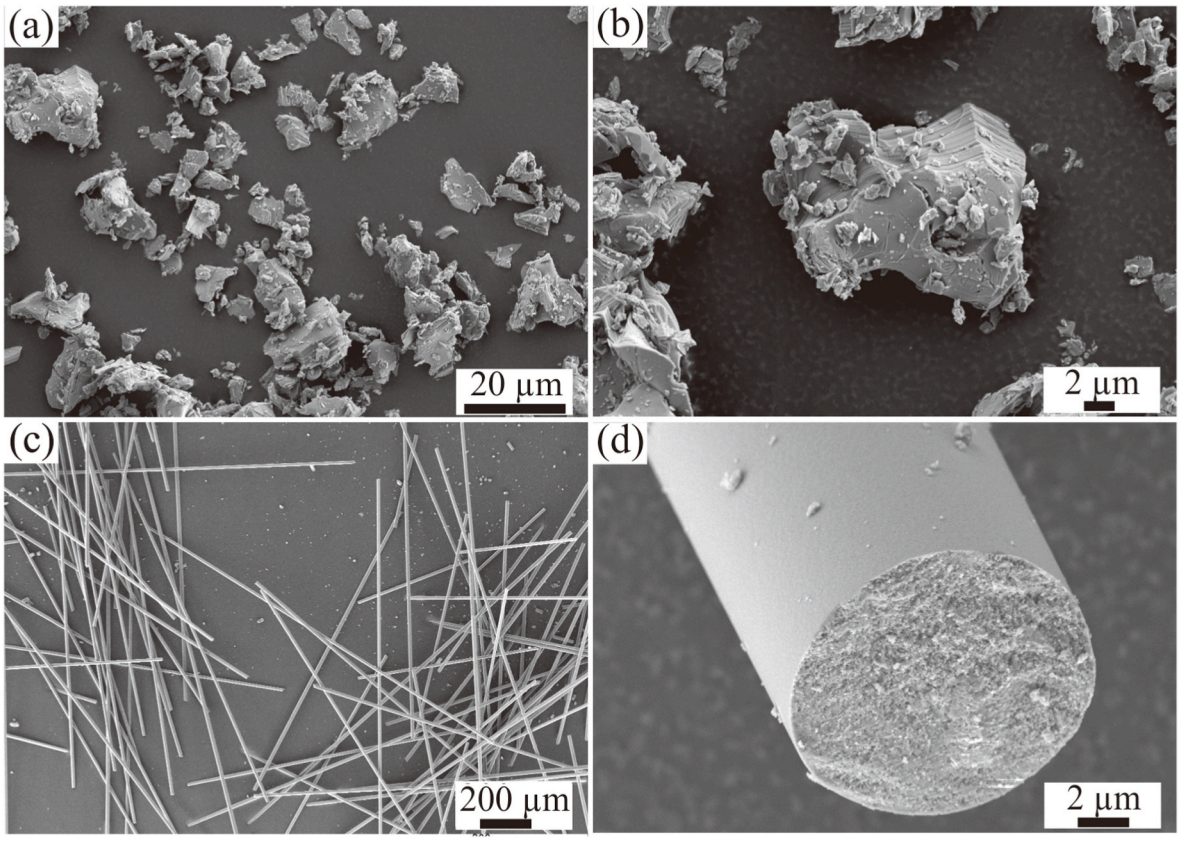

Fig. 2. SEM images of the (a–b) as-synthesized Ti_2AlN powder (c–d) hand-chopped Al_2O_3 fibers. The Ti_2AlN powders show a typical plate-like morphology and the hand-chopped Al_2O_3 fibers have an extremely large aspect ratio.

as the alignment of the fibers, on the creep deformation behavior, regarding all the as-obtained samples, TTS-type and TSS-type testing specimens were obtained by cutting using electrical discharge machining. The testing samples were cylindrical specimens with diameters of ~5 mm and heights of ~7 mm. Similar as in Ref. [17], briefly, the creep tests were carried out using an Instron 1362 electromechanical testing machine equipped with a high temperature furnace in a temperature range of 900–1200 °C under constant loads, corresponding to stress levels of 20–100 MPa. First, before the creep test, the cylindrical specimens were coated with a BN spraying agent (Boron Nitride Grade TG, 3 M Technical ceramics) on the surfaces to avoid the potential reactions between the MAX phase composites and the Al_2O_3 plates used for the mounting during the high temperature test. A compressive preload corresponding to a force of 2 N was applied to fix the specimens. Then, the samples were heated to the test temperature, using a heating rate of 5 K/min and a holding time of 1 h was applied to reach thermal equilibrium between the furnace and specimens before application of the respective constant load by the electromechanical machine. Moreover, a linear variable differential transformer (Solartron Metrology) with alumina coupling rods was utilized over the whole time to measure the displacement during the creep test. The testing temperatures and stress ranges were fixed for each individual test to the defined conditions in the range 900 °C–1200 °C and 20–100 MPa (maximum temperature limited to avoid excessive oxidation and serious deformation of the specimens), respectively. The creep tests were terminated once the steady-state deformation could be confirmed. The conditions of the creep tests are listed in detail in Table 1.

In general, the steady state creep rate can be expressed by the following equation, which depends on the testing temperature T and applied stress σ [18,23,25],:

$$\dot{\varepsilon} = \dot{\varepsilon}_0 A \left(\frac{\sigma}{\sigma_0}\right)^n \exp\left(\frac{-E_a}{RT}\right) \quad (1)$$

where A, n, Q, and R are the stress-independent constant (Dorn constant), stress exponent, activation energy for creep, and gas constant, respectively. $\dot{\varepsilon}_0$ and σ_0, which are 1 s^{-1} and 1 MPa, respectively, are used for defining the dimensions of strain rate and stress. The creep rate was determined from the slope in the secondary creep stage via a linear fitting regression analysis using Software OriginPro2018. Following Eq. (1), the activation energy E_a has been calculated from the slope of the Arrhenius plots of the creep rates of Ti_2AlN composites in air as a function of the reciprocal absolute temperatures ranging from 900 to 1200 °C under constant compressive stresses in the range of 20–100 MPa using global linear fitting of all results. Global linear fitting regression was also applied to obtain the stress exponent (n) from the double-logarithmic plots of the creep rats as a function of the applied stresses. The term 'global linear fitting' generally refers to simultaneous curve fitting operations performed on multiple plots (OriginPro2018, global fitting, parameter sharing), similar as reported in Refs. [25,28].

2.4. Microstructural characterization

The densities of the as-obtained Ti_2AlN composite specimens were characterized on the basis of the Archimedes principle using water at room temperature. The phase compositions and the amount of different phases were identified by X-ray Diffraction (XRD, D8-Discover, Bruker, US) and Rietveld refinement. The microstructure and grain distribution were characterized by field emission scanning electron microscopy (FE-SEM. Merlin, Carl Zeiss Microscopy, Oberkochen, Germany). In addition, electron backscatter diffraction (EBSD, HKL NordlysNano, Oxford Instruments, High Wycombe, UK) was employed to assess crystal

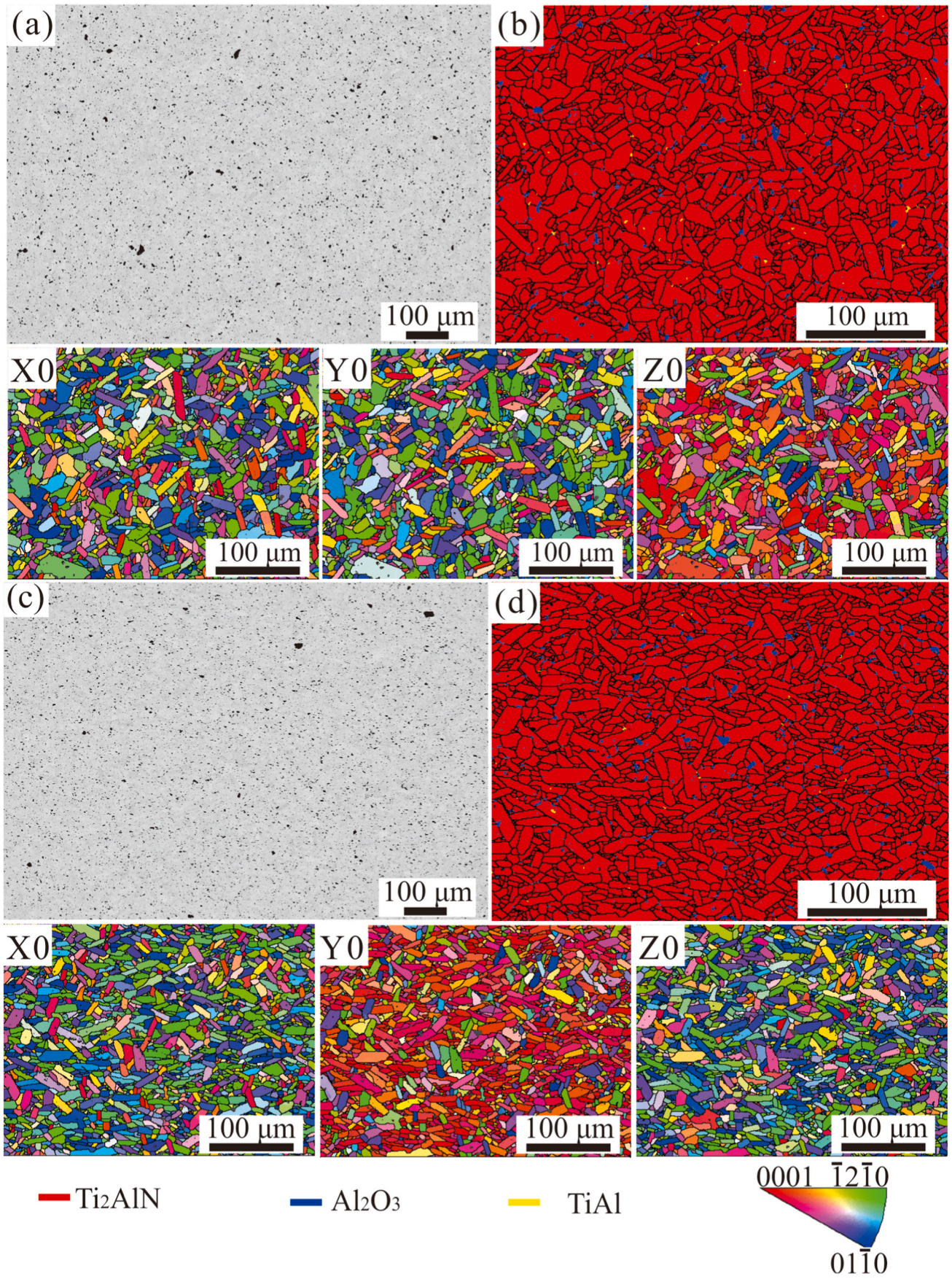

Fig. 3. SEM images and phase maps of (a–b) TTS and (c–d) TSS of 0ATN specimen and corresponding orientation maps with respect to X0, Y0 and Z0 of Ti_2AlN grains. The Al_2O_3 and TiAl particles can be observed within the Ti_2AlN matrix. Based on the orientation maps, the Ti_2AlN MAX phase grains are textured.

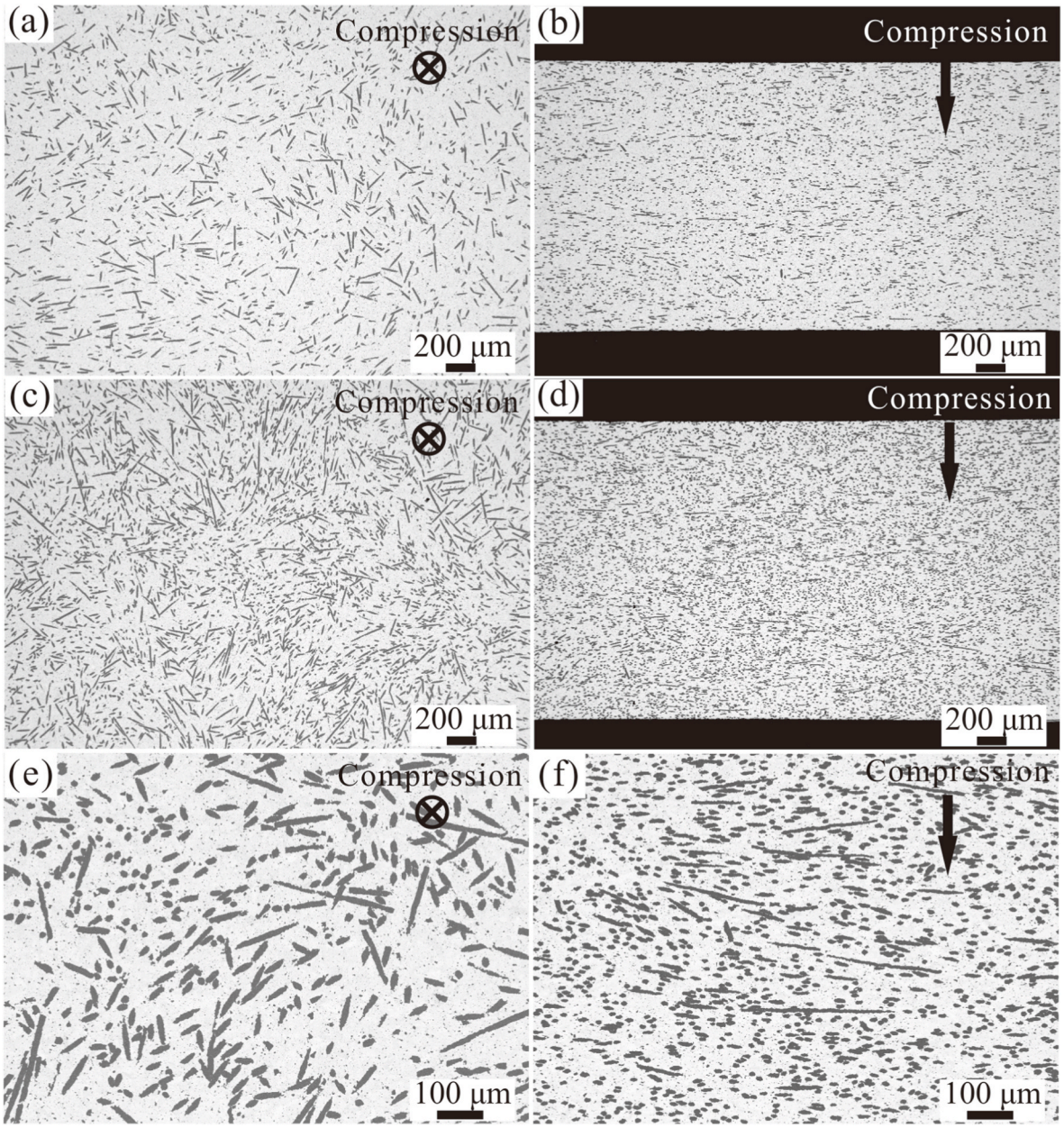

Fig. 4. SEM images of TTS and TSS for (a–b) 10ATN and (c–f) 20ATN. The dark phase corresponds to Al_2O_3 fibers, whereas the light dark phases to Ti_2AlN grains. The fiber/Ti_2AlN samples are highly dense without the presence of pores. The Al_2O_3 fibers within the composites are aligned in plane perpendicular to compression load.

orientations of the obtained Ti_2AlN samples.

3. Results and discussion

Fig. 1 presents the XRD patterns of the synthesized Ti_2AlN powder as prepared via liquid/solid state reaction. Clearly, almost all the diffraction peaks correspond to those of Ti_2AlN, implying a high purity of the as-obtained Ti_2AlN powder. In addition, the initial as-synthesized Ti_2AlN powder contains approximately 2 wt % of Al_2O_3 impurity particles as determined by Rietveld refinement from the XRD data.

Additionally, the morphologies of the as-synthesized Ti_2AlN powders after ball milling and the hand-chopped Al_2O_3 fibers after exposure to air at 750 °C for 30 min are shown in Fig. 2(a–b) and Fig. 2(c–d), respectively. The Ti_2AlN powders possess a typical plate-like morphology similar as other members of MAX phase family. The hand-chopped Al_2O_3 fibers have a diameter of ~10 μm and a rather large aspect ratio. As reported in our previous work [26], also here, commercial NaCl particles serve as the templates to retain the space/distance between Al_2O_3 fibers, avoiding the re-agglomeration after the initial ultrasonic and following magnetic stirring process. In addition, the NaCl particles might act as the 'ball milling agents' during the stirring process. Moreover, as confirmed previously, the NaCl templates are almost completely removed by water washing, thus no influence of the salt can be expected [26]. Consequently, in the current work, the existence of the NaCl salts can be ignored in the subsequent analysis.

The XRD patterns of the TTS and TSS after the FAST/SPS procedure are also shown in Fig. 1, exemplified for the 20ATN specimen. For TTS, the characterized crystal planes are mainly {00*l*} planes of Ti_2AlN, while peak intensities of other planes are not apparent. This implies that the intensities of {00*l*} planes are much larger than those of {*hk*0} planes. On the other hand, regarding TSS, the characteristic peaks of {00*l*} planes are not the only prominent peaks, since the {*hk*0} peaks are also

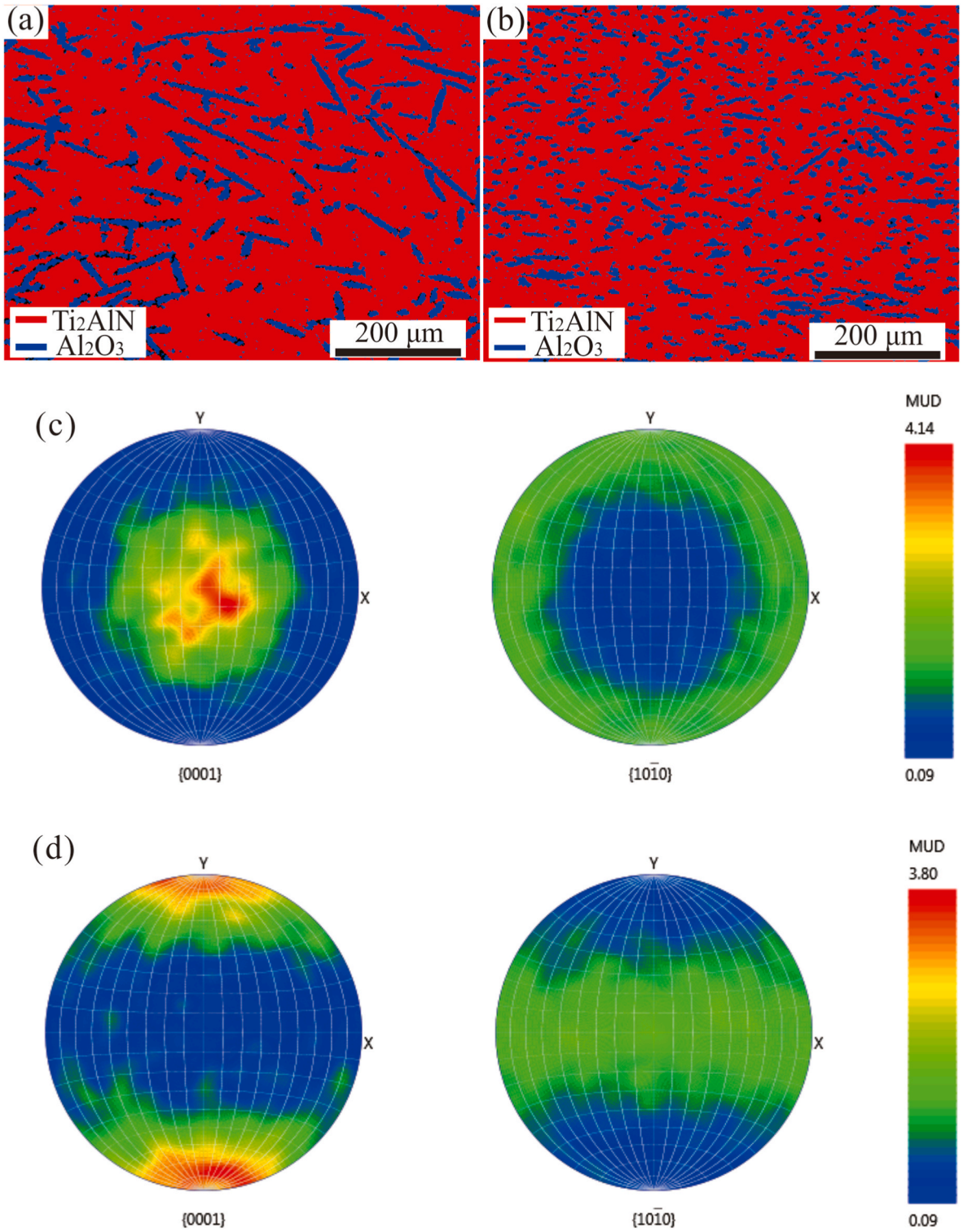

Fig. 5. Phase maps and the pole figures of (a, c) TTS and (b, d) TSS of 20ATN. The Al_2O_3 fibers are homogeneously distributed on TTS and TSS of the Ti_2AlN MAX phase matrix. In addition, the basal plane of most Ti_2AlN MAX phase grains are almost perpendicular to the compression direction based on the pole figures.

strongly increased. The {*hk*0} planes are very obvious and steep and the peaks of {*hk*0} planes are higher than those of {00*l*}. This phenomenon indicates that the 20ATN possesses a high orientation intensity along the compression direction and different grain distributions regarding TTS and TSS after FAST/SPS procedure, similar as reported in our previous work [11].

For TTS of the 20ATN specimen, (002) and (006) planes of Ti_2AlN are the main exposed crystal planes. (100) and (110) planes are the dominant peaks in the XRD patterns for TSS. Furthermore, for both TTS and TSS diffraction peaks of the Al_2O_3 fibers are also detected due to the addition of Al_2O_3 fibers with high purity (>99 wt %).

Qualitatively, the above results support the conclusion that the obtained Ti_2AlN composites are textured along the compression direction due to the fine starting powder and the type of sintering method employed for densification. As reported, the pressure applied during the sintering might be responsible for aligning the platelets of the starting

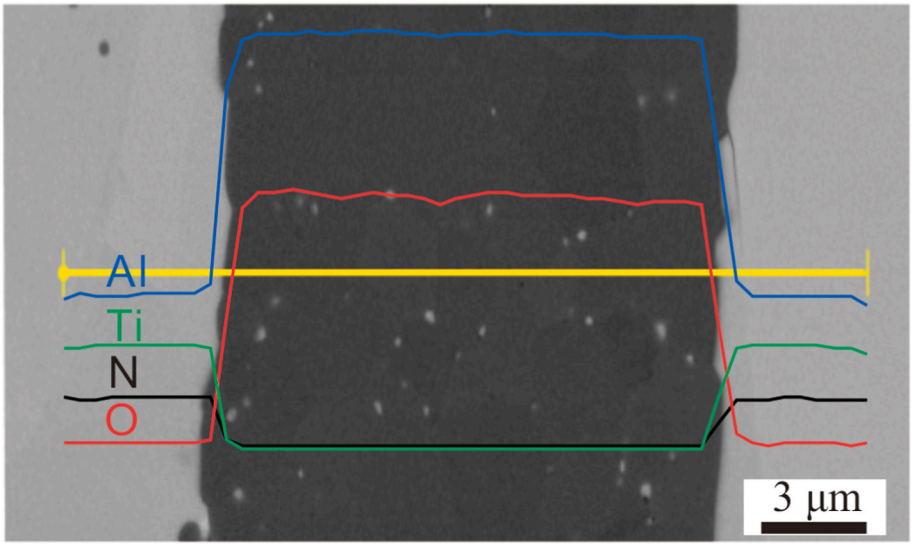

Fig. 6. EDS linear scan across an Al_2O_3 fiber on TTS of 20ATN. No reaction can be observed between Ti_2AlN matrix and Al_2O_3 fibers.

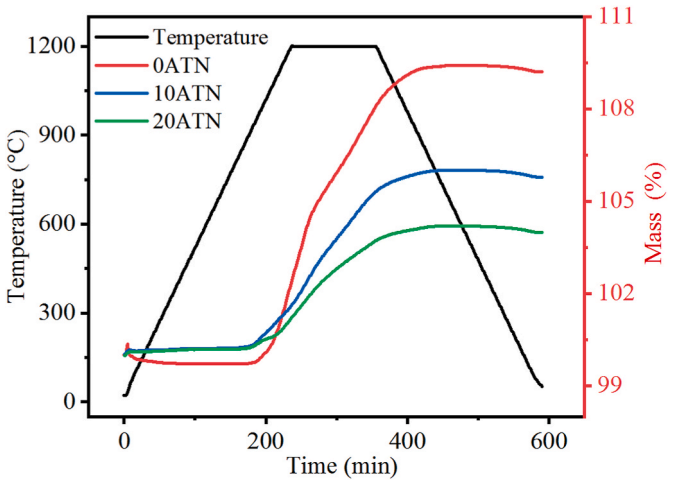

Fig. 7. Thermogravimetric analysis curves of Al_2O_3 fiber/Ti_2AlN materials. The oxidation resistance of Ti_2AlN composites was improved by the addition of Al_2O_3 fibers.

powder, resulting in a strong basal texture of TTS, whereas TSS has a mixture of prismatic and pyramidal orientations [29]. In the current work, it is obvious that for the highly textured case, the *c*-axis of Ti_2AlN MAX phase grains is close to the processing compression direction.

SEM images of TTS and TSS for the 0ATN specimen are shown in Fig. 3(a) and (c), furthermore, the corresponding phase maps as well as orientation maps are also presented in Fig. 3. Clearly, some impurities exist within the matrix, i.e. Al_2O_3 and TiAl. Based on the orientation maps, it can be concluded that the Ti_2AlN MAX phase grains are textured along the processing compression direction, which fits well with the XRD results discussed above.

Fig. 4 presents SEM images of polished TTS and TSS surfaces of the 10ATN and the 20ATN specimen. The apparent dark phase corresponds to Al_2O_3 fibers, whereas the brighter phases to Ti_2AlN grains. It is clear from these images that the Al_2O_3 fiber/Ti_2AlN composites are very dense, without pores being present. In addition, the densities of the 0ATN, 10ATN and 20ATN specimens were determined, yielding 4.279 ± 0.007, 4.239 ± 0.011 and 4.193 ± 0.007 g/cm^3, respectively. The relative densities for 0ATN, 10ATN and 20ATN were, thus, 99.50 ± 0.15, 99.51 ± 0.25 and 99.36 ± 0.18 %, respectively, considering the theoretical densities of initially formed 2 wt % Al_2O_3 particles and commercial Al_2O_3 fibers of 3.9 g/cm^3 and Ti_2AlN material of 4.31 g/cm^3. Also for these specimens, the absence of large pores and of larger quantities of small pores within the composites could be confirmed. In addition, phase maps of the 20 ATN specimen are shown in Fig. 5(a–b) to illustrate the phase distribution. As expected, for both TTS and TSS, the Al_2O_3 fibers are homogeneously distributed within the Ti_2AlN MAX phase matrix. Based on EBSD, the overall Al_2O_3 phase content on the TTS and TSS of the 20ATN specimen was 17.0 and 19.2 vol %, respectively, which in both cases is close to the initially designed nominal composition of the composite (the Ti_2AlN composite was doped with 20 vol % Al_2O_3 short fibers). This confirms an excellent homogeneity of the composites containing short Al_2O_3 fibers, even on the microscale. Therefore, the mechanical response of the composites can be studied without consideration of any influence of pores and inhomogeneity. Moreover, the basal plane of most Ti_2AlN MAX phase grains are almost perpendicular to the compression direction based on the pole figures presented in Fig. 5(c–d). Furthermore, the fibers are randomly oriented in the *x*-*y* plane with the axis of the fiber aligned along the plane, which fits well with the XRD and SEM results.

In addition, as shown in Fig. 4, the Al_2O_3 fibers within the composites are aligned in the *x*-*y* plane with the *z*-axis pointing in the normal direction. i.e. the direction along which the uniaxial pressure has been applied during the FAST/SPS procedure. The Al_2O_3 fibers appear dark because of the materials' contrast; no apparent reaction layer between the Al_2O_3 fibers and the Ti_2AlN was observed. The fibers are randomly oriented in the *x*-*y* plane with the fiber axis parallel to the plane. The length of the fibers is less than 1 mm, which suggests some fiber breakage during sintering.

Matrix/fiber interface and reactivity between them were characterized by EDS on polished specimens using a linear scan. Based on the SEM and EDS results shown in Fig. 6, no reaction effect, i.e. no formation of an interfacial layer, was observed between the Ti_2AlN matrix and Al_2O_3 fibers.

Considering all information presented above, it can be concluded that the Al_2O_3 fiber/Ti_2AlN composites obtained via FAST/SPS are textured and have different microstructure on TTS and TSS due to the pressure applied during FAST/SPS procedure. In addition, the basal planes of most MAX phase grains are almost perpendicular to the compression direction, reflecting the pronounced texture of the materials.

In order to confirm the oxidation stability, thermogravimetric analysis (TGA) curves of different Al_2O_3 fiber/Ti_2AlN materials are

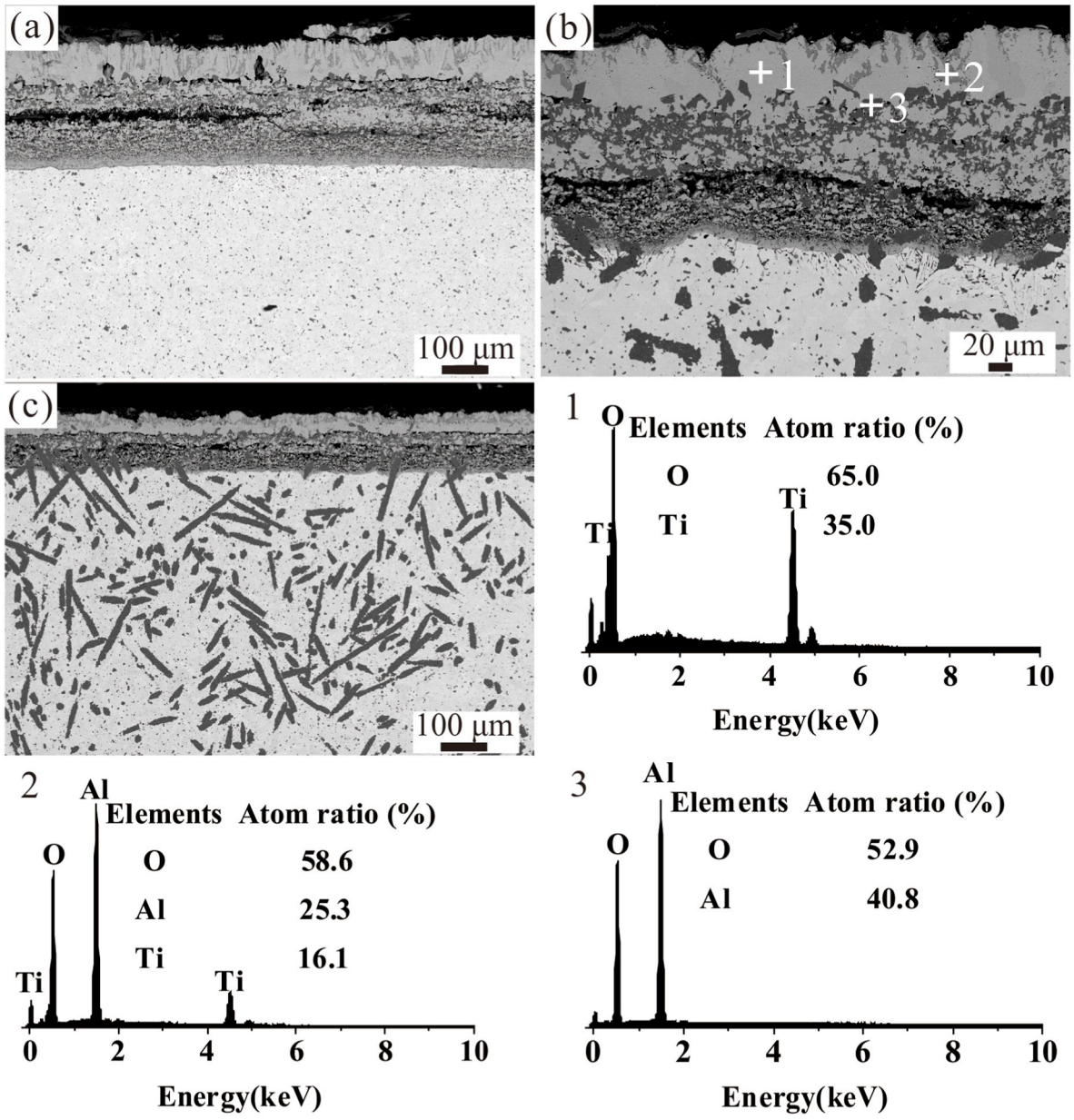

Fig. 8. SEM images of the oxide scale of oxidized (a) 0ATN, (b) 10ATN and (c) 20ATN. The thickness of oxide scale of 0ATN, 10ATN and 20ATN was determined to be in a range of ~270–310 μm, ~160–200 μm and ~110–130 μm, respectively, demonstrating the positive influence of the addition of short Al_2O_3 fibers on the oxidation resistance.

presented in Fig. 7. After the TGA tests of Ti_2AlN materials at 1200 °C, the mass gains for 0ATN, 10ATN and 20ATN specimens reached 9.4, 6.0 and 4.2 wt %, respectively. Additionally, the microstructures of the oxide layer are shown in Fig. 8. The thickness of the oxide layer of the 0ATN, 10ATN and 20ATN specimen was determined to be in a range of ~270–310 μm, ~160–200 μm and ~110–130 μm, respectively, demonstrating an apparent positive influence of the addition of short Al_2O_3 fibers on the oxidation resistance, which fits well with the TGA results shown in Fig. 7. In addition, the oxide layer was composed of TiO_2, Al_2O_3, and Al_2TiO_5, as shown in the EDS results in Fig. 8. Considering the stability and excellent oxidation resistance of Al_2O_3 fiber, it can prevent the further oxidation of MAX phase matrix, therefore, the oxidation resistance of the Ti_2AlN materials was improved with the increasing of the addition of Al_2O_3 fibers. Since the materials exhibit excellent oxidation resistance up to 1200 °C, oxidation effects can be neglected in the following creep analysis.

As typical example, the strain vs time graph presented in Fig. 9 contain both primary and secondary creep contributions. However, the analysis is only based on an analysis of the secondary creep. The activation energies and stress exponents of all the Ti_2AlN composites characterized in the current work are summarized in Table 2, being based on the Arrhenius plots in Fig. 10.

As shown in Table 2, the experimentally determined stress exponents are comparable within limits of the experimental uncertainties for all the specimens tested at temperatures in the range from 900 to 1200 °C, indicating that the creep behavior of TTS-type and TSS-type specimens is mainly governed by the creep property of Ti_2AlN matrix. Thus, the rate-controlling mechanism for creep deformation can be assumed to be the same for TTS-type and TSS-type Al_2O_3 fiber/Ti_2AlN specimens under the applied test conditions. No obvious difference of activation energies of TTS-type specimens can be observed, especially considering the experimental uncertainties. By contrast, the activation energies determined for the TSS-type specimens increase with the addition of Al_2O_3 fibers, implying more energy is needed initiate creep deformation when more

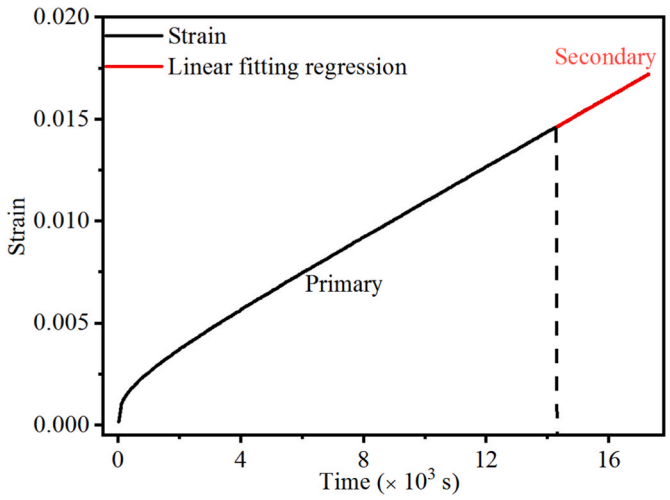

Fig. 9. Typical creep deformation behavior of TTS-type 20ATN testing specimen performed at 1200 °C under 40 MPa. The two regimes, i.e. primary creep and secondary creep, can be clearly distinguished.

Table 2
Summary of creep activation energy and stress exponents of Al_2O_3 fiber/Ti_2AlN composites.

Specimen		E_a (kJ/mol)	n
0ATN	TTS-type	253 ± 12	1.4 ± 0.1
	TSS-type	294 ± 24	1.3 ± 0.1
10ATN	TTS-type	267 ± 14	1.7 ± 0.2
	TSS-type	308 ± 15	1.3 ± 0.1
20ATN	TTS-type	272 ± 15	1.3 ± 0.1
	TSS-type	362 ± 13	1.6 ± 0.1

Al_2O_3 fibers are present parallel to the compression direction within the composites.

It should be noted that the obtained creep behavior is a result of several factors, including the Ti_2AlN matrix, the content of Al_2O_3 fibers, grain boundaries of Ti_2AlN grains and the interfaces between Ti_2AlN grains and Al_2O_3 fibers, the orientation of Al_2O_3 fibers, which will be discussed in more detail in the following.

3.1. The contribution of Ti_2AlN matrix

The calculated stress exponents for TTS-type and TSS-type 0ATN are 1.4 ± 0.1 and 1.3 ± 0.1, respectively, indicating grain boundary sliding (GBS) as creep controlling mechanism. Thus, the texture does not appear to influence the creep mechanism at the temperatures in the range from 900 to 1200 °C, which are temperatures that are close to and/or higher than the apparent brittle-to-ductile transformation (BDT) temperatures; the MAX phases investigated to date exhibit a BDT behavior between 800 °C and 1100 °C [30,31]. The absence of a change in the expected BDT range in the current work is similar to that reported in previous work [28]. Furthermore, the values reported here are also similar to those reported for bulk Ti_2AlN materials fabricated via reactive FAST/SPS [25].

The morphology of the crept 0ATN material is shown in Fig. 11(a–d). Cleary, after the creep test, de-cohesion of MAX phase grains can be observed, confirming GBS as the predominant creep mechanism. Therefore, grain boundaries are easy to de-bond during the compressive creep tests. Note, it cannot be ruled out that grain boundaries de-bond during the compressive creep tests; however, even using the advanced microstructural characterization illustrated in the current work signs of de-bonding could not be verified, perhaps also indicating that at these elevated temperatures re-binding occurs. Apparent de-bounding of grain boundaries could lead to a redistribution of stress along grain boundaries and respective atomic movement and changes of the apparent grain boundary microstructure; such aspects should be the focus of future studies. In addition, as demonstrated in the schematic illustration shown in Fig. 11(e), during the creep test, cracks formed at the triple junctions related to the GBS and/or grain rotation, which agrees well with the microstructural investigation results on the crept 0ATN specimen shown in Fig. 11(a–d).

The creep rates of TSS-type 0ATN specimens are slightly higher than those of TTS-type 0ATN specimens, which has also been observed for textured Ti_2AlC and Ti_3AlC_2 in our previous work [28]. This might be related to the higher numbers of grain boundaries representing an easy diffusion path along the compression direction due to the textured structure within the specimens. Considering all presented above, it can be concluded that the textured structure influences the creep rates, but not the creep mechanism.

3.2. The contribution of Al_2O_3 fibers

As shown in Fig. 10, clearly, the creep rates of all TTS-type specimens are comparable, implying that the addition of Al_2O_3 fibers has no significant impact on the creep behavior for the TTS-type specimens. Regarding TSS-type specimens, interestingly, TSS-type 20ATN exhibits the lowest creep rates compared to TSS-type 0ATN and TSS-type 10ATN specimens under the same test conditions. Furthermore, the creep behavior of TSS-type 0ATN material has also been improved via the addition of 10 vol % Al_2O_3 fibers, considering the higher creep rates of TSS-type 0ATN. Therefore, an improvement of the creep behavior, i.e. a reduction of the creep rates, is achieved for TSS-type specimens by the introduction of Al_2O_3 fibers. TSS-type 20ATN has the best creep resistance among all the test specimens, while TSS-type 0ATN yielded the highest creep rates, indicating that the addition of 20 vol % Al_2O_3 fibers can significantly improve the compressive creep resistance for TSS-type specimens. As shown in Fig. 12, for crept 10 ATN and 20 ATN specimens, de-cohesion within the matrix resulting from the GBS and grain rotation appears to be inhibited by the addition of Al_2O_3 fibers. Furthermore, cracks appear to be stopped by the interfaces between Al_2O_3 fibers and Ti_2AlN grains.

Such an effect might be related to the higher stiffness of the fibers, as more energy would be needed for de-bonding of the interfaces and further crack propagation. As a result, the addition of Al_2O_3 fibers can improve the creep resistance of Ti_2AlN materials.

As shown in Fig. 10, the creep rates of TSS-type specimens decreased with the addition of Al_2O_3 fibers, while no obvious difference of creep rates for TTS-type specimens was observed, indicating a positive impact of the Al_2O_3 fibers on the creep resistance for TSS-type specimens, thus demonstrating the significance of orientation of fibers on the creep resistance.

According to the creep behavior of TTS-type and TSS-type specimens, the orientation of the Al_2O_3 fibers along the applied loads can improve the creep resistance of MAX phase materials, resulting from the higher strength of the interface between Ti_2AlN grains and Al_2O_3 fibers compared to the strength of the Ti_2AlN grains as well as from the existence of more interfaces along the compression direction. Therefore, during the application of the compression loads, the GBS and/or de-cohesion occurred first and further deformation then resulted in the de-bonding of the interfaces between Ti_2AlN grains and Al_2O_3 fibers, which needs more energy for the de-bonding.

In addition, as reported [32], the creep resistance will be improved when the fibers are parallel to the loading directions due to the transfer of the applied stress to the Al_2O_3 fibers. The fibers then inhibit the lateral deformation of the Ti_2AlN matrix along the fibers. While for the TTS-type 20ATN, where Al_2O_3 fibers were mainly distributed in the plane perpendicular to the applied load, the load transfer did not occur. Only crack inhibition contributed to improve the creep resistance to some extent. In contrast to the behavior of MAX phase grain boundaries,

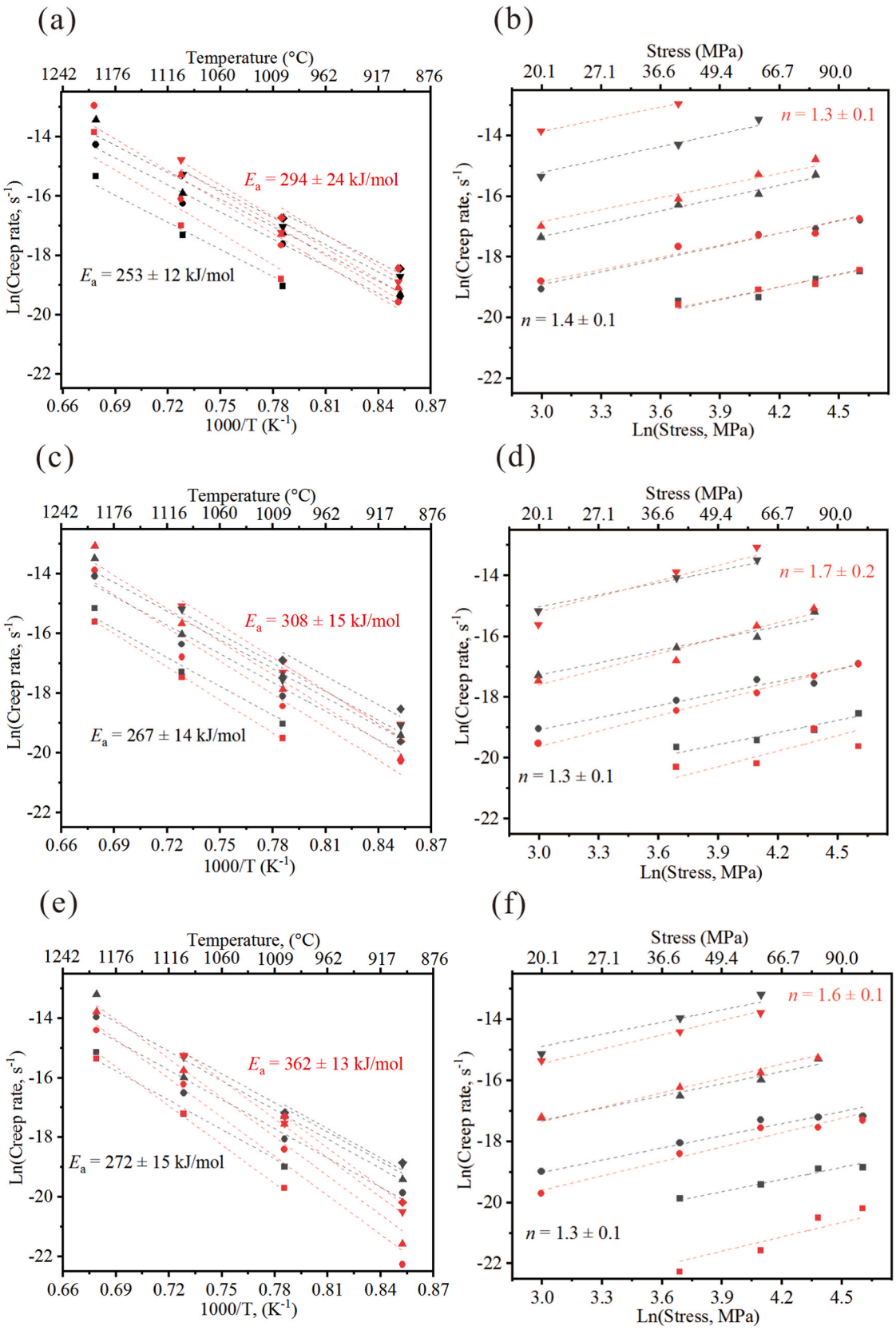

Fig. 10. Arrhenius plots of the creep rates as a function of inverse temperature and the ln-ln plots of creep rate as a function of applied compressive stress of (a–b) 0ATN, (c–d) 10ATN and (e–f) 20ATN in the temperature range of 1000–1200 °C under applied the stresses from 20 MPa to 100 MPa. The black lines and red lines refer to the data of TTS-type and TSS-type specimens, respectively. The activation energy E_a and stress exponents n were obtained using global linear fitting regression. (For interpretation of the references to colour in this figure legend, the reader is referred to the Web version of this article.)

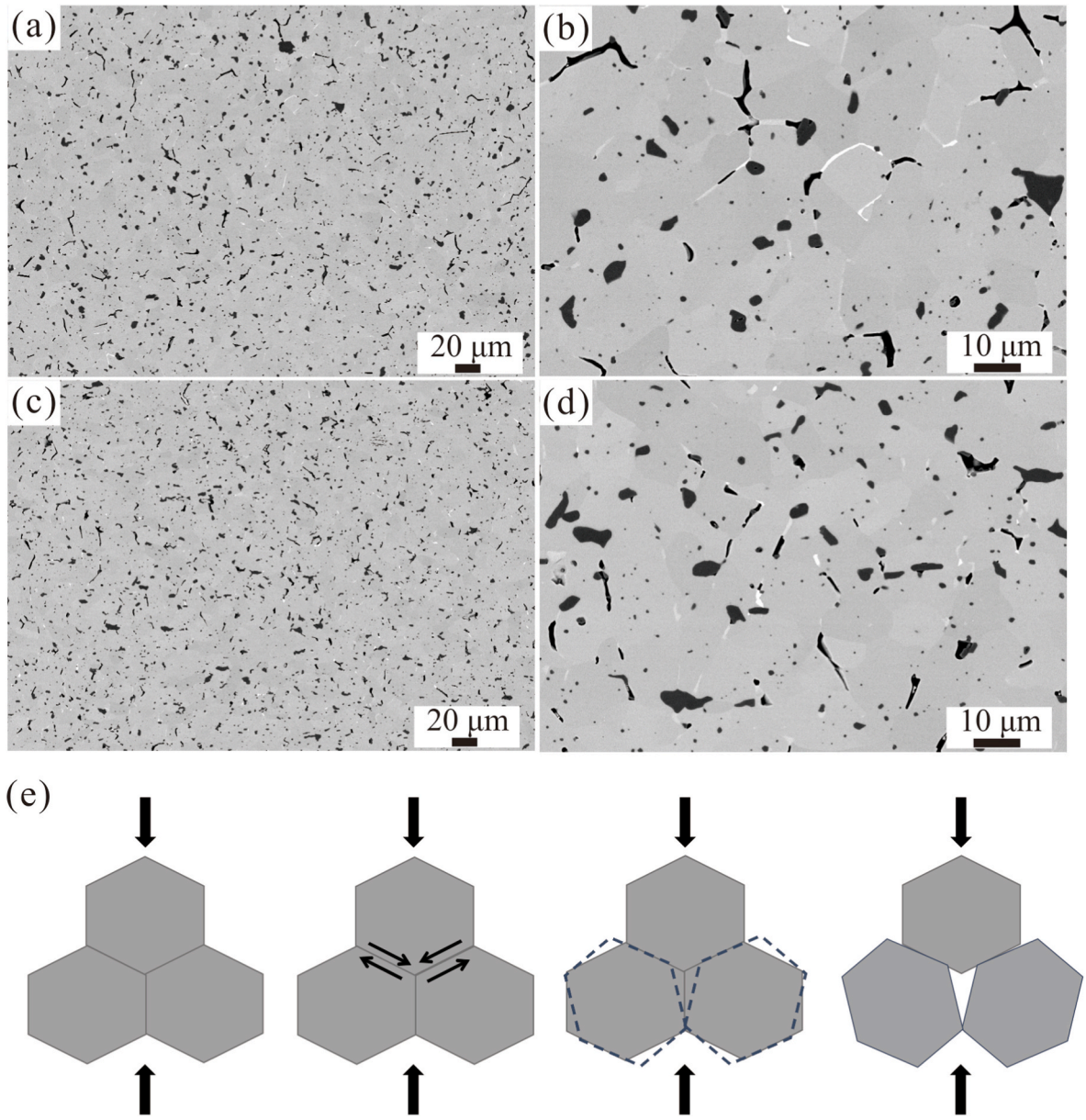

Fig. 11. SEM images of the crept (a–b) TTS-type (c–d) TSS-type 0ATN, and (e) the schematic illustration of grain boundary sliding and gain rotation of Ti_2AlN gains during compressive creep test. The delamination and de-cohesion of the MAX phase grains were observed, illustrating GBS as the predominant creep mechanism.

the interfaces between Al_2O_3 fibers and the matrix contributed significantly to the creep resistance. In addition, more interfaces existed within TSS-type 20ATN along the compression direction due to the higher content of Al_2O_3 fibers. Therefore, the addition of Al_2O_3 fibers will result in a more obvious impact on the improvement of creep resistance for TSS-type specimens and TSS-type 20ATN specimen has the best creep resistance. Accordingly, creep deformation will be more difficult with the addition of Al_2O_3 fibers for TSS-type Ti_2AlN materials, which fits well with an increase of the experimentally determined activation energies for TSS-type specimens.

Based on the discussion above, the textured microstructures, stronger interfaces and the orientation of the fibers are crucial for the improvement of the creep resistance of Al_2O_3 fiber/Ti_2AlN composites.

4. Conclusion

Dense composites of Al_2O_3 fiber/Ti_2AlN were fabricated via a NaCl salt templated strategy and FAST/SPS procedure with anisotropic grain distribution and fiber alignment. The oxidation resistance of Ti_2AlN composites was improved by the addition of Al_2O_3 fibers, and higher fractions of Al_2O_3 fibers resulted in better oxidation resistance. Also the creep behavior shows improvement due to the addition of Al_2O_3 fibers. Overall, the creep observed in the samples can be attributed to grain boundary sliding and the Ti_2AlN grains with basal plane perpendicular to the loading direction exhibited better creep resistance. The alignment of Al_2O_3 fibers parallel to the loading direction enhances the creep resistance due to the load transfer and the existence of more interfaces with stronger bonding along the compression direction. In summary, this work provides an explanation of the improved oxidation and deformation behavior of fiber/MAX phase composites at elevated temperatures, thereby aiding further future materials improvement regarding a better long-term high temperature stability.

Declaration of competing interest

The authors declare that they have no known competing financial

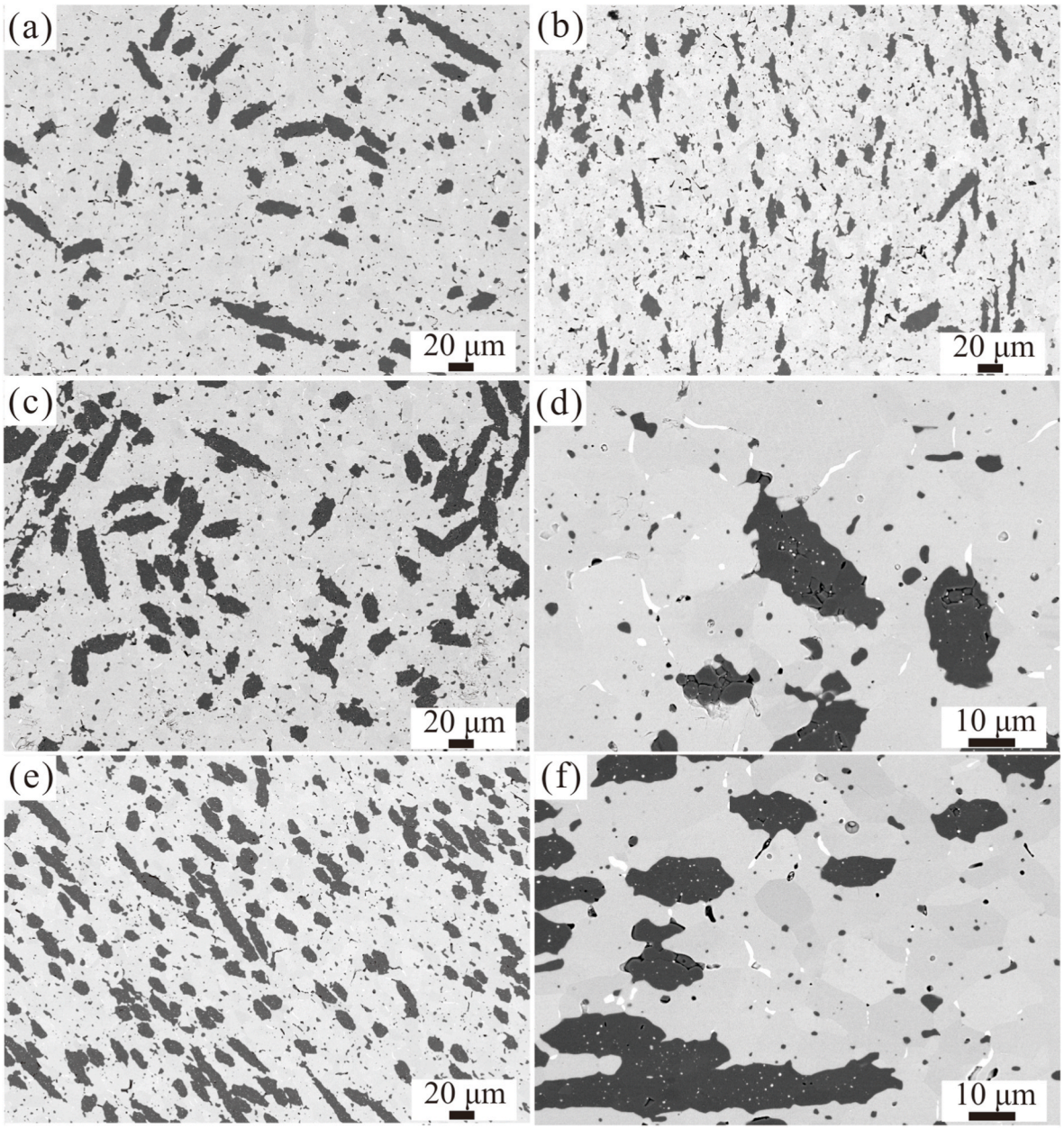

Fig. 12. SEM images of the crept (a) TTS-type 10ATN (b) TSS-type 10ATN, (c–d) TTS-type 20ATN and (e–f) TSS-type 20ATN. The cracks within the matrix resulting from the GBS and grain rotation can be inhibited by the addition of Al_2O_3 fibers. And the cracks were hindered by the interface between Al_2O_3 fibers and Ti_2AlN grains which contributed significantly to the creep resistance.

interests or personal relationships that could have appeared to influence the work reported in this paper.

Acknowledgements

The authors would like to thank Ms. T. Osipova for supporting the creep tests, Dr. D. Grüner for microstructural investigation via SEM, and Mr. M. Ziegner for supporting the work with XRD investigations. Mr. X. Li gratefully acknowledges the support from the China Scholarship Council of China (201808440373). Prof. Dr. J. Gonzalez-Julian thanks the financial support by the Germany's Federal Ministry of Education and Research ("Bundesministerium für Bildung und Forschung") under the MAXCOM project (03SF0534).

References

[1] M.W. Barsoum, M. Radovic, Elastic and mechanical properties of the MAX phases, Annu. Rev. Mater. Sci. 41 (1) (2011) 195–227.
[2] J. Gonzalez-Julian, Processing of MAX phases: from synthesis to applications, J. Am. Ceram. Soc. 104 (2) (2020) 659–690.
[3] Z.M. Sun, Progress in research and development on MAX phases: a family of layered ternary compounds, Int. Mater. Rev. 56 (3) (2013) 143–166.
[4] M.W. Barsoum, The $M_{n+1}AX_n$ phases: a new class of solids; thermodynamically stable nanolaminates, Prog. Solid State Chem. 28 (2000) 201–281.
[5] A.-S. Farle, C. Kwakernaak, S. van der Zwaag, W.G. Sloof, A conceptual study into the potential of $M_{n+1}AX_n$-phase ceramics for self-healing of crack damage, J. Eur. Ceram. Soc. 35 (1) (2015) 37–45.
[6] D.J. Tallman, B. Anasori, M.W. Barsoum, A critical review of the oxidation of Ti_2AlC, Ti_3AlC_2 and Cr_2AlC in air, Mater. Res. Lett. 1 (3) (2013) 115–125.
[7] S. Guo, C. Hu, H. Gao, Y. Tanaka, Y. Kagawa, SiC(SCS-6) fiber-reinforced Ti_3AlC_2 matrix composites: interfacial characterization and mechanical behavior, J. Eur. Ceram. Soc. 35 (5) (2015) 1375–1384.
[8] S. Guo, Fiber size effects on mechanical behaviours of SiC fibres-reinforced Ti_3AlC_2 matrix composites, J. Eur. Ceram. Soc. 37 (15) (2017) 5099–5104.

[9] S. Guo, Improvement of mechanical properties of SiC(SCS-6) fibre-reinforced Ti_3AlC_2 matrix composites with Ti barrier layer, J. Eur. Ceram. Soc. 36 (6) (2016) 1349–1358.
[10] P. Tao, W. Liu, Y. Wang, Fabrication of SiC_f/Ti_3SiC_2 composites with high thermal conductivity by spark plasma sintering, Ceram. Int. 46 (2) (2020) 2571–2575.
[11] A. Dash, J. Malzbender, R. Vaßen, O. Guillon, J. Gonzalez-Julian, Short SiC fiber/Ti_3SiC_2 MAX phase composites: fabrication and creep evaluation, J. Am. Ceram. Soc. 103 (2020) 7072–7081.
[12] J. Gonzalez-Julian, J. Llorente, M. Bram, M. Belmonte, O. Guillon, Novel Cr_2AlC MAX-phase/SiC fiber composites: synthesis, processing and tribological response, J. Eur. Ceram. Soc. 37 (2) (2017) 467–475.
[13] C.B. Spencer, J.M. Córdoba, N. Obando, A. Sakulich, M. Radovic, M. Odén, L. Hultman, M.W. Barsoum, Y. Zhou, Phase evaluation in Al_2O_3 fiber-reinforced Ti_2AlC during sintering in the 1300 °C-1500 °C temperature range, J. Am. Ceram. Soc. 94 (10) (2011) 3327–3334.
[14] M.A. Lagos, C. Pellegrini, I. Agote, N. Azurmendi, J. Barcena, M. Parco, L. Silvestroni, L. Zoli, D. Sciti, Ti_3SiC_2-C_f composites by spark plasma sintering: processing, microstructure and thermo-mechanical properties, J. Eur. Ceram. Soc. 39 (9) (2019) 2824–2830.
[15] J. Gonzalez-Julian, I. Kraleva, M. Belmonte, F. Jung, T. Gries, R. Bermejo, Multifunctional performance of Ti_2AlC MAX phase/2D braided alumina fiber laminates, J. Am. Ceram. Soc. 105 (1) (2021) 120–130.
[16] X. Liu, J. Xue, F. Yang, F. Ye, X. Fan, L. Cheng, Design and fabrication of Al_2O_{3f}/SiCN composite with excellent microwave absorbing and mechanical properties, J. Am. Ceram. Soc. 103 (11) (2020) 6255–6264.
[17] Y. Zou, F. Schulze-Küppers, M. Balaguer, J. Malzbender, M. Krüger, Creep behavior of porous $La_{0.6}Sr_{0.4}Co_{0.2}Fe_{0.8}O_{3-\delta}$ substrate material for oxygen separation application, J. Eur. Ceram. Soc. 38 (4) (2018) 1702–1710.
[18] M. Radovic, M.W. Barsoum, T. El-Raghy, S.M. Wiederhorn, Tensile creep of coarse-grained Ti_3SiC_2 in the 1000–1200 °C temperature range, J. Alloys Compd. 361 (1–2) (2003) 299–312.
[19] M. Radovic, M.W. Barsoum, T. El-Raghy, S.M. Wiederhorn, Tensile creep of fine-grained (3-5 μm) Ti_3SiC_2 in the 1000-1200 °C temperature range, Acta Mater. 49 (2001) 4103–4112.
[20] T. Zhen, M.W. Barsoum, S.R. Kalidindi, M. Radovic, Z.M. Sun, T. El-Raghy, Compressive creep of fine and coarse-grained T_3SiC_2 in air in the 1100–1300 °C temperature range, Acta Mater. 53 (19) (2005) 4963–4973.
[21] D.J. Tallman, M. Naguib, B. Anasori, M.W. Barsoum, Tensile creep of Ti_2AlC in air in the temperature range 1000–1150 °C, Scripta Mater. 66 (10) (2012) 805–808.
[22] E. Drouelle, A. Joulain, J. Cormier, V. Gauthier-Brunet, P. Villechaise, S. Dubois, P. Sallot, Deformation mechanisms during high temperature tensile creep of Ti_3AlC_2 MAX phase, J. Alloys Compd. 693 (2017) 622–630.
[23] W. Araki, J. Gonzalez-Julian, J. Malzbender, High temperature compressive creep of dense and porous Cr_2AlC in air, J. Eur. Ceram. Soc. 39 (13) (2019) 3660–3667.
[24] A. Dash, J. Malzbender, K. Dash, M. Rasinski, R. Vaßen, O. Guillon, J. Gonzalez-Julian, Compressive creep of SiC whisker/Ti_3SiC_2 composites at high temperature in air, J. Am. Ceram. Soc. 103 (10) (2020) 5952–5965.
[25] X. Li, J. Gonzalez-Julian, J. Malzbender, Fabrication and mechanical performance of Ti_2AlN prepared by FAST/SPS, J. Eur. Ceram. Soc. 40 (13) (2020) 4445–4453.
[26] X. Li, X. Zhao, J. Gonzalez-Julian, J. Malzbender, Salt-templated strategy for well dispersed multi-component composites with morphologies ranging from millimeter to nano-scale, Compos. Commun. 27 (2021), 100862.
[27] X. Li, J. Malzbender, G. Yan, J. Gonzalez-Julian, R. Schwaiger, A combined experimental and modeling study revealing the anisotropic mechanical response of Ti_2AlN MAX phase, J. Eur. Ceram. Soc. 41 (12) (2021) 5872–5881.
[28] X. Li, X. Xie, J. Gonzalez-Julian, R. Yang, R. Schwaiger, J. Malzbender, Oxidation and creep behavior of textured Ti_2AlC and Ti_3AlC_2, J. Eur. Ceram. Soc. 42 (2) (2022) 364–375.
[29] X. Li, X. Xie, J. Gonzalez-Julian, J. Malzbender, R. Yang, Mechanical and oxidation behavior of textured Ti_2AlC and Ti_3AlC_2 MAX phase materials, J. Eur. Ceram. Soc. 40 (15) (2020) 5258–5271.
[30] M. Barsoum, T. El-Raghy, The MAX phases: unique new carbide and nitride materials, Am. Sci. 89 (4) (2001).
[31] A. Guitton, A. Joulain, L. Thilly, C. Tromas, Evidence of dislocation cross-slip in MAX phase deformed at high temperature, Sci. Rep. 4 (2014) 6358.
[32] Z. Deng, Effect of different fiber orientations on compressive creep behavior of SiC fiber-reinforced mullite matrix composites, J. Eur. Ceram. Soc. 19 (12) (1999) 2133–2144.